A NETWORK OF SURFACE PRESSURE OBSERVATIONS TO CONSTRAIN AEROSOL FORCING IN MARS CLIMATE MODELS

R. J. Wilson, *NASA Ames Research Center, Moffett Field CA, USA, (Robert.j.Wilson@nasa.gov)*, **M.A. Kahre,** *NASA Ames Research Center, Moffett Field CA, USA.*

Introduction: The evolving distribution of radiatively active dust and water ice clouds plays a major role in modulating the seasonal and interannual variation in the thermal forcing of the Martian atmosphere. Thermal tides are the global-scale atmospheric response to the diurnally varying thermal forcing due to aerosol heating within the atmosphere and radiative and convective heat transfer from the surface. The tide includes westward propagating (sun-synchronous) waves driven in response to solar heating, as well as nonmigrating waves that result from zonal variations in the thermotidal forcing caused by variations in topography and surface thermal properties and in the distribution of aerosols (dust and water ice clouds).

The migrating tides are of particular interest, since they are generally directly responsive to the aerosol distribution. However, distinguishing these tides from the mix of additional nonmigrating tides is difficult with only a limited number of surface observations. For example, Figure 1 shows the seasonal evolution of the amplitude of the diurnal (S_1) and semidiurnal (S_2) harmonics of surface pressure observed by the Rover Environmental Monitoring Station (REMS) aboard the MSL rover Curiosity in Gale crater (4.5°S, 137°E) for Mars Years 33 and 34. The figure highlights the very close correlation between the amplitude of S_2 and the evolving global column dust opacity during the MY34 global dust storm. By contrast, the observed S_1 response is less easily interpreted, and is surprisingly strong at the start of the regional dust storm at $L_s = 323°$ while the S_2 response remains relatively weak, consistent with the global opacity.

The recent acquisition of surface pressure data by the Mars2020 mission in Jezero crater (18.5°N, 77.2°E) provides longitude coverage in the tropics, that complements the 5-year MSL record, the four-year record at Viking Lander 1 (VL1 at 22.5°N, 312°E), and the 1+year record at InSight (4.5°N, 135°E). The notable lack of interannual variability in Martian climate during the aphelion season (L_s=0-135°) allows these sets of lander data to be considered as a 4-station tropical network (Figure 2).

This presentation will describe an approach by which a global perspective of the evolving tide response can be gained through the use of high-resolution Mars global climate model (MGCM) simulations. A better understanding of the global and local scale influences on the diurnal variability of surface pressure is critical for detailed comparisons between atmospheric models and observations.

MGCMs include parameterizations that yield a thermal forcing field from distributions of dust and water ice clouds. Simulated atmospheric temperature and surface pressure are then obtained consistently as the atmosphere responds to the thermal forcing. The extent to which the simulated fields correspond to observations provides insight into how well the thermal forcing field is represented. It has become evident that radiative forcing by water ice clouds contributes significantly to the thermal balance particularly in the aphelion season, although details are still poorly constrained. Another poorly constrained issue is the effect of vertical variation of dust (detached dust layers) on thermal forcing. A better understanding of the global and local scale influences on the diurnal variability of surface pressure is critical for detailed comparisons between atmospheric models and observations. A network would be a most effective way to accomplish this.

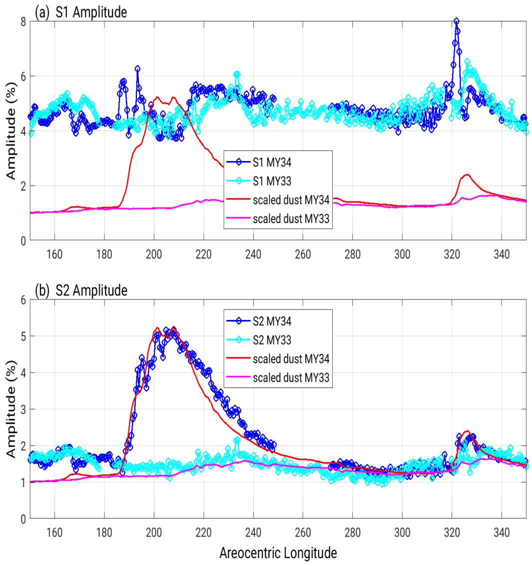

Figure 1. (a) The seasonal variation of the diurnal tide amplitude S_1 at the MSL site for MY34 (blue) and MY33 (cyan). Amplitudes are normalized by the local diurnal-mean surface pressure. (b) As above but for the semidiurnal tide, S_2 at the MSL site. The tropical (30°S-30°N) zonal-mean column dust visible opacity variations (from DGDM climatology) are shown as red and magenta lines for MY34 and MY33, respectively. The opacity has been scaled (τ_{scale}= 0.9τ+ 0.75) to emphasize the close correlation with S_2.

Thermal Tides and Aerosol Forcing: An observed tide harmonic, S_n, at a lander site represents the sum over all zonal wavenumbers, including the corresponding migrating component and additional eastward and westward propagating nonmigrating components. Migrating tides include DW1, SW2, TW3, and QW4, respectively for the westward propagating diurnal, semidiurnal, terdiurnal, and quad-diurnal migrating tides. There is roughly a linear relationship between the SW2 amplitude and the dust column optical depth, which makes this mode an effective proxy for globally integrated thermal forcing. Moreover, due to the meridionally broad and vertically deep structure of the dominant Hough mode associated with SW2, the pressure response is relatively insensitive to the details of the vertical and latitude distribution of thermal forcing. By contrast, the surface pressure response of the migrating diurnal tide DW1 is weaker for a vertically extended dust distribution than for a more shallowly confined distribution with equivalent column optical depth. Thus, elevated dust layers or water ice clouds could have an influence on the observed S_1 response.

The most prominent nonmigrating tides are the resonantly enhanced, eastward propagating diurnal and semidiurnal Kelvin waves, DE1 and SE2, with zonal wavenumbers 1 and 2, respectively. These waves are forced by zonal wave 2 and 4 components of thermal forcing, including the influence of topography and aerosol [*Wilson and Hamilton*, 1996]. Discussion of the influence of longitude variations of aerosol on DE1 is deferred to a later section.

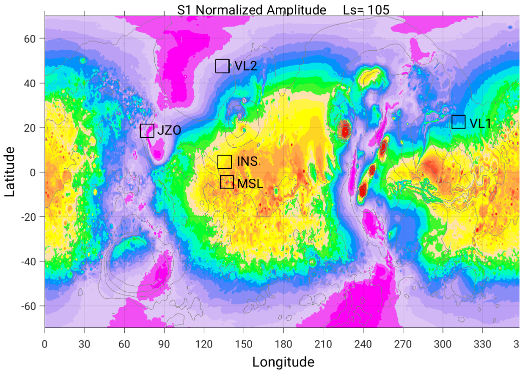

Figure 2. (a) The simulated spatial variation of normalized diurnal pressure variability, S_1, in % of diurnal-mean surface pressure for Ls= 105°. The locations of MSL, InSight, Mars 2020, VL1 and VL2 are indicated. The prominent zonal wave 2 modulation is due to the interference between the westward (DW1) and eastward (DE1) diurnal tide components.

MGCM Simulations: We have been using a very high-resolution version of the NASA Ames MGCM to simulate diurnal variability in surface pressure at scales ranging from that of Gale crater to the planetary scale, thus distinguishing the pressure signature of local topographically driven circulations from that of the global tide. The results from the predecessor GFDL version of the model are presented in *Wilson et al*. (2017). More recent simulations of the MSL tides during the MY34 global dust storm are described in a manuscript in preparation.

The NASA Ames MGCM uses a finite volume dynamical core in a cubed-sphere geometry, which enables very high resolution simulations on a relatively uniform grid. The physics included in the MGCM are described in *Kahre et al*. (*this meeting*). Briefly, we include many options for the handling of dust and water ice clouds, including highly controlled prescriptions for their distributions and radiative effects. We have performed such simulations (C48 and C384) to examine the local and global-scale surface pressure responses. The C384 simulation has a resolution of 0.25° x 0.25° (~15 km). We have annual simulations at both resolutions. As we show below, the MGCM does reasonably well at capturing many of the tide al components discussed here.

Figure 2 shows the spatial distribution of normalized S_1 amplitude at L_s=105° in a C384 simulation. The large-scale response is dominated by a combination of DW1 and DE1, yielding the prominent zonal wave 2 modulation in diurnal tide amplitude. In the same season, there is a strong zonal wave 4 pattern in the S_2 response (not shown), seen in previous simulation studies [*Wilson and Hamilton*, 1996; *Guzewich et al*., 2016].

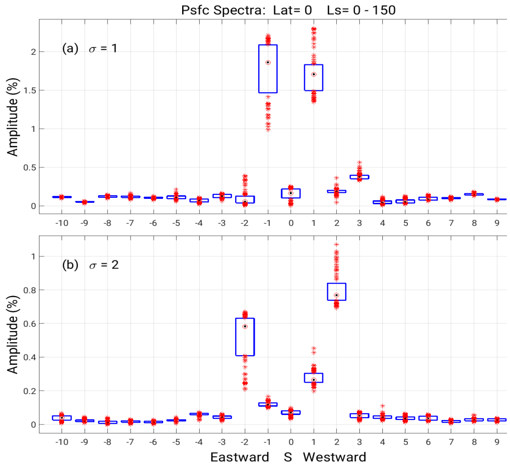

Figure 3. Box plots of equatorial tide mode amplitudes from the C384 simulation of the aphelion season derived from a space-time spectral analysis identifying eastward and westward propagating diurnal (top) and semidiurnal (bottom) components. The vertical extent of the blue boxes spans the range of the middle two quartiles of amplitude over the L_s=0-150° period, while red stars represent the outlier values. The DW1/DE1 pair dominates the diurnal tide (S_1) variability while the SW2/SE2 pair dominates the semidiurnal tide (S_2) variability.

Figure 3 shows the results of a space-time analyis of the simulated equatorial surface pressure field, indicating the range of amplitudes of the eastward and westward propagating components of the equatorial diurnal and semidiurnal pressure fields in the L_s = 0-150° season. It is evident that the dominant contributions to S_1 structure and seasonal variability are associated with the DW1/DE1 pair of tide modes, with smaller contributions from other waves, including DW2 and DW3. Similarly, the SW2/SE2 pair dominates the structure and variability of S_2 in the aphelion season, with a lesser contribution from SW1. The meridional structures for both pairs of tide modes are quite broad so that changes in component amplitudes and phases would be reflected in similar tide changes throughout the tropics. MGCM simulations support the expectation that the migrating tide (SW2) accounts for the majority of the S_2 response during dustier seasons.

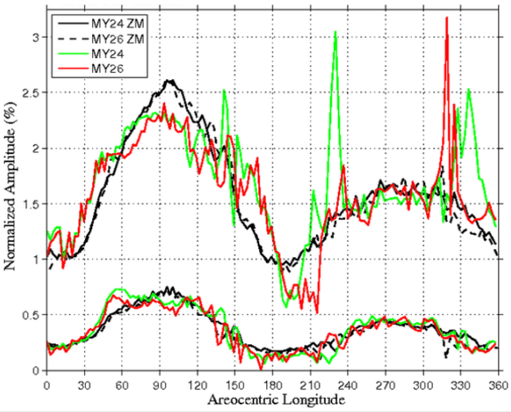

Figure 4. Simulations of DE1 and SE2 tide equatorial amplitudes with realistic dust scenarios for MY24 and MY26 (green and red, respectively). The black curves show results using zonally averaged dust scenarios

Figure 4 illustrates the sensitivity of the DE1 response to the zonal variations in dust. Two simulations were carried out using the seasonally-varying but zonally averaged dust column scenarios for MY24 and MY26 compiled by Montabone et al. (2015).

These yield nearly identical and smoothly varying seasonal variations in equatorial DE1 and SE1 in spite of the differing histories of regional dust storms in the two Mars years. The seasonal variation of the resonantly-enhanced Kelvin waves (DE1 and SE2) show a strong preference for the two solstice seasons, with a clear emphasis on the $L_s = 90°$ season. Re-running the simulations with the fully variable dust scenarios yields substantial variability in the DE1 response that is associated with changes to the zonal wave 2 distribution of column dust. These variations are particularly strong at the onset of the pre- and post-solstice regional storms. The 3 storm events associated with the Chyrse channel lead to significant amplification of DE1, while the Isidis flushing event at L_s=208° in MY26 results in the phasing of the zonal wave-2 component of the dust pattern that suppresses the DE1 response. It is likely that rapid DE1 amplification is present at the start of the two dust storm events seen in Figure 1 during MY34. There are systematic, though weaker influences on the DE1 response in the aphelion season. The simulations did not include water ice clouds and it is reasonable to anticipate that zonal variations in the tropical water ice cloud belt could induce changes as well.

Aphelion Season Observations: The amplitudes and phases of diurnal and semidiurnal pressure harmonics at the 4 network sites are shown in Figure 5. The synchronized decline and increase in S_2 amplitude centered about L_s =90° at VL1, INS, and MSL is due to the destructive interference between SW2 and SE1 at their two longitudes, separated by 180 degrees. By contrast, S_2 has a relative maximum around solstice at Jezero crater due to constructive interference between SW2 and SE2. Figure 6 shows a comparison of simulated results with the observations for the amplitude of S_1. Similar comparisons can be made with the amplitudes and phases of S_2 and higher order harmonics. The simulation permits consideration of the constituent tide modes. The model tends to overpredict the amplitude of S_1. This is attributed to an overly strong DW1 response, which likely is due to the absence of upper level heating associated with radiatively active water ice clouds. The diurnal Kelvin wave (DE1) is also likely somewhat too strong, as suggested by the mismatch in amplitude (and phase, not show) at Jezero crater. The simulation indicates that the difference in S_1 amplitude between MSL and INS is largely due to the large-scale influence of the Mars dichotomy on DW1 and the local-scale influence of Gale crater; both enhance the response at MSL (4.5°S) vs InSight (4.5°N).

Ongoing Research and Conclusions: We are carrying out a fitting procedure where the network observations are used to calculate amplitudes and phases of DW1, DE1, SW2, and SE2 that yield improved estimates of the amplitudes and phases of S_1 and S_2 in the actual Mars atmosphere. We take advantage of the predicted meridional structure of modes to be fitted, thus setting up a least squares fit for their amplitude and phases as they evolve through the aphelion season. We have also been examining the sensitivity of the tide response to aspects of the aerosol forcing like the strength of the water ice cloud heating, and the vertical distribution of dust and water ice clouds. Thus we anticipate that good estimates of the isolated amplitudes of these diagnostic tide modes will provide useful guidance on assessing the radiative forcing by dust and water ice clouds.

References

Guzewich, S.D., et al. (2016), Atmospheric tides in Gale crater, *Icarus, 268*, 37-49,

Kahre et al., (2022). 7th MAMO Conference, Paris, France. June 14-17, 2022.

Montabone et al., (2015), Eight-year climatology of dust on Mars. *Icarus*.

Wilson, R.J., and K.P. Hamilton (1996), Comprehensive model simulation of thermal tides in the martian atmosphere, *J. Atmos. Sci*. 53, 1290-1326.

Wilson, R.J., J.M. Murphy, and D. Tyler (2017), Assessing atmospheric thermal forcing from surface pressure data; Separating thermal tides and local topographic influence Sixth International Workshop on the Mars Atmosphere: Modeling and Observations, Granada, Spain, Jan 17-20, 2017. http://www-mars.lmd.jussieu.fr/granada2017/abstracts/wilson_granada2017.pdf

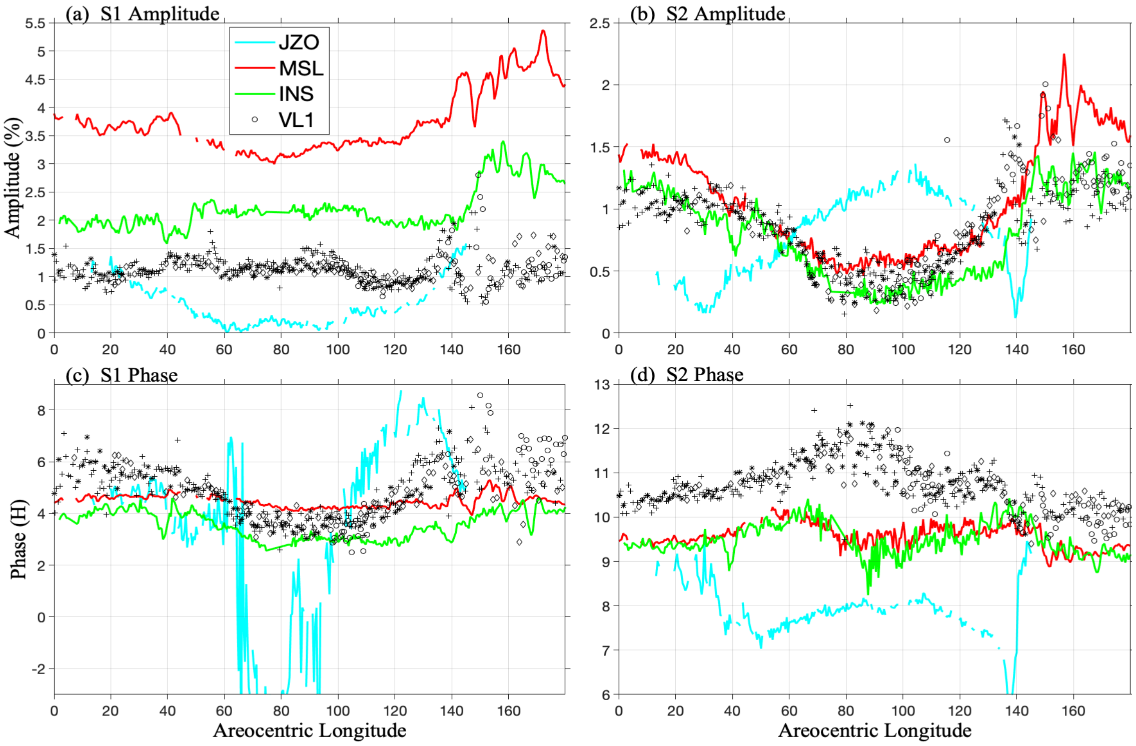

Figure 5. (a) Observations of the normalized diurnal harmonic amplitude of surface pressure, S_1 at 4 sites on the Martian surface. These include Mars2020 (JZO, MY36, in cyan), MSL (MY33, in red), InSight (INS, green) and Viking Lander 1 (VL1, 4 years, in black) (b) Semidiurnal tide amplitude, S_2. (c) Diurnal tide phase. (d) Semidiurnal tide phase.

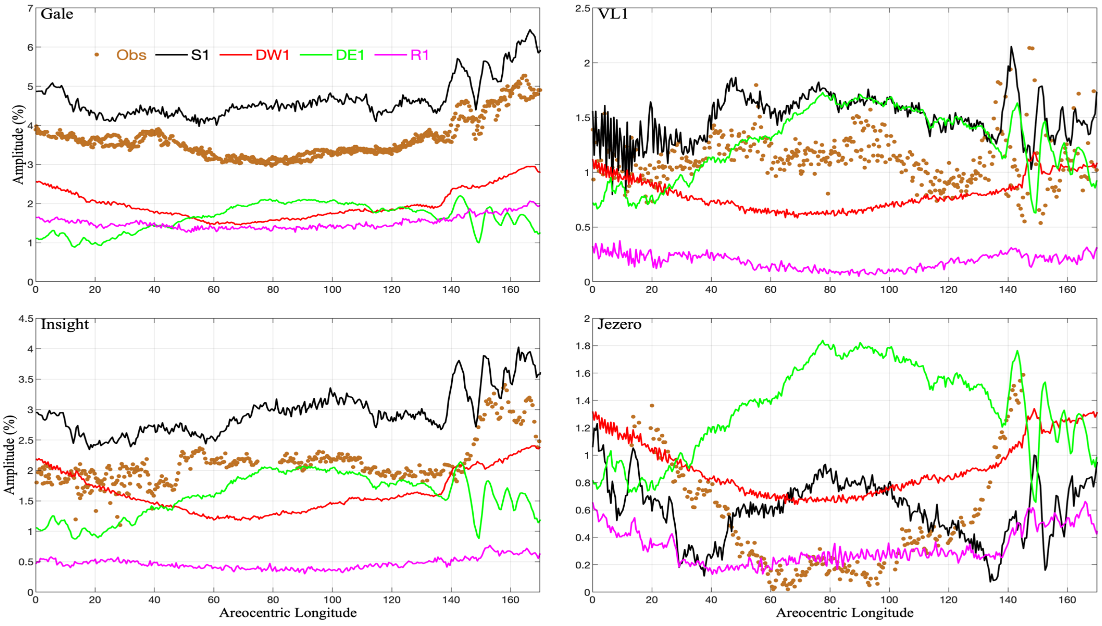

Figure 6. (a) Comparison of simulated S_1 tide amplitude (black line) with observations by MSL in Gale crater (in brown). Also shown are the simulated seasonally-varying DW1(red) and DE1 (green) amplitudes at the latitude of the lander. The magenta curve (R1) is the amplitude contribution attributed to the localized topographic response (defined in *Wilson et al*. 2017). Note that wave phase needs to be considered in combining wave component contributions to the tide signal at a given longitude. (b) Simulation results for VL1. (c) Simulation results for InSight. (d) Simulation results for Mars2020 in Jezero crater.